11-1998

Photofragmentation of Third-row Hydrides Following Photoexcitation at Deep-core Levels

D. L. Hansen
University of Nevada, Las Vegas

M. E. Arrasate
University of Nevada, Las Vegas

J. Cotter
University of Nevada, Reno

G. R. Fisher
Lawrence Berkeley National Laboratory

Oliver Hemmers
University of Nevada, Las Vegas, Oliver.Hemmers@unlv.edu
Follow this and additional works at: https://digitalscholarship.unlv.edu/hrc_xray_atomic_molecular

Part of the Atomic, Molecular and Optical Physics Commons
See next page for additional authors

Repository Citation

Authors

D. L. Hansen, M. E. Arrasate, J. Cotter, G. R. Fisher, Oliver Hemmers, K. T. Leung, Jon C. Levin, R. Martin, Paul Neill, Rupert C. Perera, I. A. Sellin, Marc Simon, Y. Uehara, B. Vanderford, S. B. Whitfield, and Dennis W. Lindle

Photofragmentation of third-row hydrides following photoexcitation at deep-core levels

D. L. Hansen,[1] M. E. Arrasate,[1] J. Cotter,[2] G. R. Fisher,[3] O. Hemmers,[1] K. T. Leung,[4] J. C. Levin,[5] R. Martin,[1] P. Neill,[2]
R. C. C. Perera,[3] I. A. Sellin,[5] M. Simon,[6] Y. Uehara,[7] B. Vanderford,[1] S. B. Whitfield,[8] and D. W. Lindle[1]

[1]*Department of Chemistry, University of Nevada, Las Vegas, Nevada 89154-4003*
[2]*Department of Physics, University of Nevada, Reno, Nevada 89557-0058*
[3]*Lawrence Berkeley National Laboratory, Berkeley, California 94720*
[4]*Department of Chemistry, University of Waterloo, Waterloo, Ontario, Canada N2L 3G1*
[5]*Department of Physics, University of Tennessee, Knoxville, Tennessee 37996*
[6]*Laboratoire pour l'Utilisation du Rayonnement Electromagnetique, Bâtiment 209D, Université Paris–Sud, 91405 Orsay Cedex, France*
and Commissariat à l'Energie Atomique, Département de Recherche sur l'État Condensé, les Atom et les Molécules, Service des
Photons, Atomes et Molécules, Bâtiment 522, CEN Saclay, 91191 Gif-sur-Yvette Cedex, France
[7]*Mitsubishi Electric Corporation, Amagasaki, Hyogo 661, Japan*
[8]*Department of Physics and Astronomy, University of Wisconsin, Eau Claire, Wisconsin 54702*
(Received 12 June 1998)

The relaxation dynamics of HCl, DCl, H_2S, and D_2S following photoexcitation in the vicinities of the Cl and S K-shell thresholds (~ 2.8 keV for Cl, ~ 2.5 keV for S) were studied by means of ion time-of-flight mass spectroscopy. In all cases, the onset of pre-edge core-shell photoionization precedes the formation on resonance of a significant amount of neutral hydrogen as well as postcollision-interaction effects above threshold. Examination of the width of the H^+ peak in spectra taken with the analyzer parallel and perpendicular to the polarization vector of the incident light indicates that on resonance, the photofragmentation asymmetry parameter, β, is approximately two for HCl, and is clearly positive for H_2S. [S1050-2947(98)08211-0]

PACS number(s): 33.80.Gj, 33.80.Eh

Time-of-flight mass spectroscopy and coincidence measurements of atoms and molecules are relatively well-understood techniques [1–3]. Coupled with the high brightness and high resolution of synchrotron-radiation (SR) sources, these techniques have proven useful in elucidating some of the multitude of electronic and fragmentation decay pathways available to core-excited systems. To date, the vast majority of these studies have concentrated on relaxation of systems following excitation of a shallow-core electron, where shallow-core levels are those that can decay electronically only through interaction with valence-shell electrons (e.g., Cl $2p$, Br $3d$). In contrast, the present measurements focus on deep-core-level excitations (i.e., Cl $1s$, S $1s$). Deep-core holes have shorter lifetimes and typically relax through Auger decay to create shallow-core holes. Because of this extra decay step, deep-core-excited systems have a much wider array of pathways by which they can relax and usually produce much more highly charged residual ions by means of a stepwise series of decays known as a vacancy cascade [4].

Gas-phase HCl and H_2S serve as interesting systems to study for a number of reasons. In both cases, the core-level spectroscopy is well understood [5–7], and electron-spectroscopy measurements [8–12] following shallow-core-level excitation have been performed. Both molecules are also isoelectronic with Ar for which ion-spectroscopy measurements following K-shell excitation are available [13–15], thus allowing a useful comparison between atomic and molecular decay pathways. Because HCl and H_2S are chemically identical to DCl and D_2S, it is also useful to study the deuterated systems in order to determine the changes in fragmentation kinematics that result.

I. EXPERIMENT

The experiments were performed using soft-x-ray SR from beamline 9.3.1 at the Advanced Light Source (ALS) in Berkeley, California [16–18], and at the National Institute of Standards and Technology/Argonne National Laboratory beamline X-24A at the National Synchrotron Light Source (NSLS) in Brookhaven, New York [19,20]. Beamline 9.3.1 at the ALS is a bending magnet beamline covering the 2–6 keV (6–2 Å) photon-energy range. It provides a flux of 10^{11} photons s^{-1} in a narrow bandpass (≤ 0.5 eV) by means of a two-crystal [Si(111)] ''Cowan-type'' monochromator. Focusing is provided by a pair of matched toroidal mirrors before and after the monochromator. At beamline X-24A, a similar double-crystal monochromator provides a resolution $E/\Delta E = 5000–10\,000$ in the 2–6-keV photon-energy range. A toroidal mirror downstream from the monochromator provides focusing, while a spherical mirror upstream collimates the beam and limits the amount of power incident on the first monochromator crystal. Both beamlines deliver a soft-x-ray beam with a brightness of $10^{10}–10^{12}$ photons s^{-1} mm^{-2} mrad^{-2} eV^{-1}.

Photon-energy calibration is achieved by scanning the monochromator through the $1s$ threshold region while monitoring the total-ion yield (Fig. 1) with the TOF analyzer. Comparing features, particularly subthreshold resonances, in these absorptionlike spectra to previously measured photoabsorption results [5–7] determines the photon energy with an accuracy of ± 0.2 eV. Calibration is checked periodically over the course of an experiment to compensate for small drifts (< 1 eV) primarily caused by heating of the first crystals of the monochromators [20].

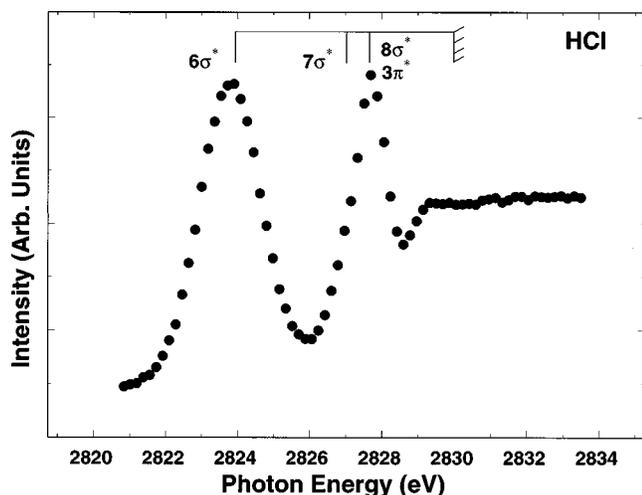The time-of-flight mass spectrometer (Fig. 2) is divided

FIG. 1. Total-ion-yield spectrum for HCl.

FIG. 3. Argon spectrum taken at a photon energy above the *K*-shell threshold (3205 eV) at beamline 9.3.1 during ALS two-bunch operation. See text for an explanation of *x*-axis scaling.

by stainless-steel plates into five regions of differing width and electric field strength. In the center of each plate is an aperture covered with high-transmission (90%) conducting wire mesh to minimize field distortions. The first region, between the pusher plate and first grid, is referred to as the extraction region. It is here that a hollow grounded needle serves as an effusive source of the gas under study. The pusher plate and first grid are held at approximately equal but opposite voltages, providing a uniform electric field with only a minimal distortion due to the needle.

The second, third, and fourth regions are referred to as the first-acceleration, drift, and second-acceleration regions, respectively. As the names imply, the acceleration regions are areas of constant electric field through which the ions are accelerated, while the drift region is field-free. The fifth and final region is a short, field-free buffer region immediately before the microchannel plates (MCPs), which serves to prevent feedback into the extraction region of electrons produced by ion impact on the MCPs, thus minimizing nonphotoionization events.

The width and field strength of each region of the time-of-flight mass spectrometer is optimized for the 656-ns orbital period of the ALS while maintaining spatial resolution through space focusing [1]. In addition, acceleration voltages
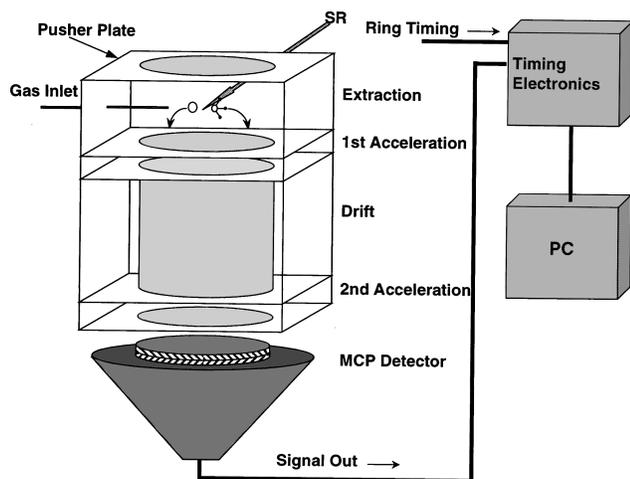

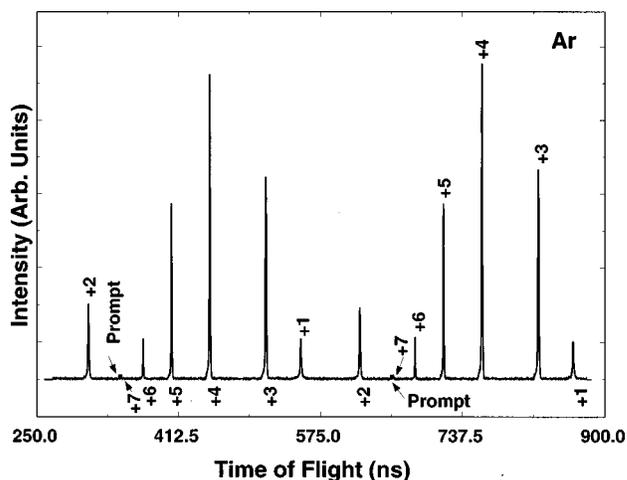FIG. 2. The ion time-of-flight mass spectrometer.

and discriminator settings are selected to ensure uniform detection efficiency for all ions and charge states [13]. The ion-TOF mass spectrometer has apertures of 254 mm, the active diameter of the MCPs. Simulations suggest that at nominal operating voltages, there is no discrimination against ions created at the tip of the needle and ejected perpendicular to the analyzer axis with kinetic energies up to 50 eV. In order to determine the effect of ion angular distribution on collection efficiency, ion-TOF data were taken with the axis of the analyzer both parallel (0°) and perpendicular (90°) to the polarization vector of the SR. Branching ratios of ionic fragments from HCl and H_2S are nearly identical for the two analyzer orientations, indicating that angular discrimination in the detection of ions, especially H^+, is negligible.

Ion detection is accomplished using two MCPs in a chevron configuration. The MCP signal is collected by a 50-Ω matched-impedance conical anode (Galileo Corporation, model TOF 2003). The pulse from the conical anode is sent through a preamplifier, if necessary, then to a constant-fraction discriminator (CFD), which provides a time-to-amplitude converter (TAC) with a logic pulse whose timing is unaffected by the signal amplitude. The TAC serves as a nanosecond stopwatch to determine flight times of individual ions with respect to the SR orbital pulse signal and outputs an analog signal to an analog-to-digital converter (ADC) with amplitude proportional to the time difference between the start and stop signals provided to the TAC. The ADC converts the signal to a digital number and transmits it to a multichannel analyzer.

The experimental setup was tested at the ALS. Results for Ar are shown in Fig. 3. Because of the double-bunch mode of operation at the ALS, two spectra, indicated by labels above or below the baseline, respectively, are observed. The time axis gives the correct flight times for peaks with labels below the spectrum. Flight times for all peaks in the second spectrum (labels above) are shifted by +328 ns, the time separation between two ALS bunches. The ultimate timing resolution for the experiment can be determined from the widths of the prompt peaks resulting from light scattered from the sample onto the detector. These peaks, which have
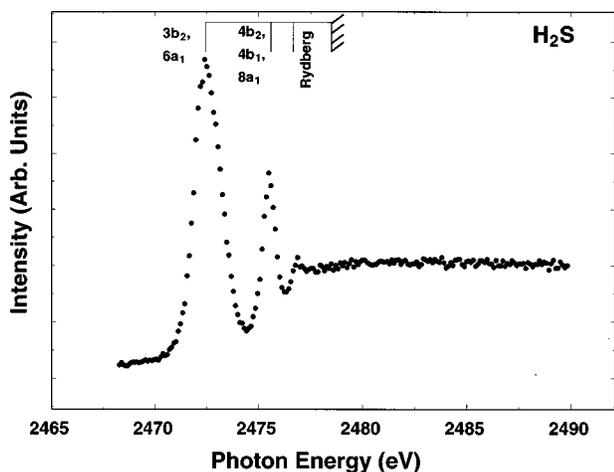
FIG. 4. Total-coincidence-yield spectrum for H_2S.

a flight time near zero, have a full width at half maximum (FWHM) of only 200 ps. The most intense peak in the spectrum, Ar^{4+}, has a FWHM of 840 ps, while Ar^{7+}, the most efficiently space-focused peak, has a 600-ps FWHM. The high time resolution observed is a result of the excellent timing characteristics of the ALS and is an indication that the analyzer design and construction were successful in achieving good resolution [18].

There are four modes of data collection with the ion-TOF mass spectrometer: total-ion yield (TIY), singles, total-coincident-ion yield (TCY), and photoion-photoion coincidence (PIPICO). Total-ion yield spectra are recorded by scanning the monochromator around the ionization threshold energy for a core-shell electron of the species under study. The total number of ions detected is recorded as a function of photon energy, producing a photoabsorptionlike curve (Fig. 1). Interactions that result in relaxation through fluorescence only are not recorded, however; this is only a small fraction of the total number of interaction events ($<1\%$). Total-coincident-ion-yield curves are taken in a similar manner monitoring the total number of coincidences between two ions from the same molecule (Fig. 4).

In the ''singles'' mode, time-of-flight spectra (Fig. 5) are collected with only one or two electron bunches circulating
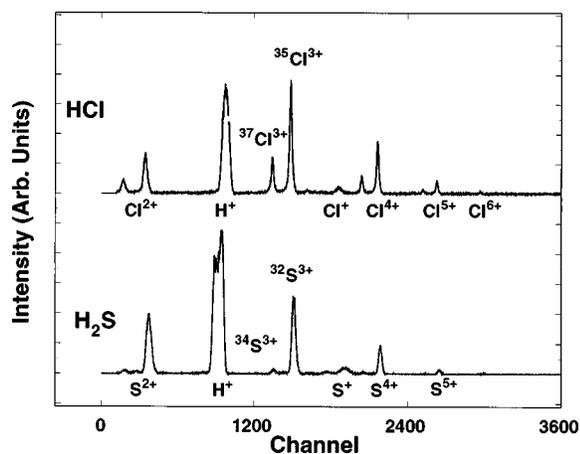

FIG. 5. TOF singles spectra of HCl and H_2S taken above the Cl 1s and S 1s thresholds, respectively. Two isotopes of chlorine and sulfur are visible.

in the storage ring. The start pulse for the timing circuit is provided by the detection of an individual ion, and the ring timing pulse, produced by the periodic pulsing of the SR (328 ns for ALS two-bunch, 567 ns at NSLS), provides the stop signal. Thus the ion-TOF singles spectra are inverted relative to actual flight times (i.e., slower ions appear to the left). In addition, because the ALS operates in 2-bunch mode, peaks due to the slowest ions ''wrap around'' in the narrower time window. The singles spectra in Fig. 5 show that photofragmentation dominates and that the fragment atoms often have a high degree of ionization. Indeed, the molecular ions HCl^+ and DCl^+ are a product of less than 1% of the photointeractions, and the molecular ion HS^+ is produced in fewer than 3%. These spectra also provide an indication of the resolution of the spectrometer. For HCl (Fig. 5) and DCl (not shown), the isotopes ^{35}Cl (75.77%) and ^{37}Cl (24.23%) are well resolved. The isotopes ^{32}S (95.02%) and ^{34}S (4.21%) are also easily distinguished in H_2S spectra (Fig. 5). Because ions are measured in coincidence with the SR signal, this method has an advantage over electron-ion coincidence measurements because there is no need to correct for differences in detection efficiency that arise from the differing numbers of free electrons associated with different charge states [21].

In the PIPICO mode of operation, two ions from the same molecule provide the start and stop signals for the timing circuit (in this work H^+ provides the start, and Cl^{n+} or S^{n+} provides the stop). Thus the difference in flight time between two ions is measured, and the operation mode of the storage ring is irrelevant. These measurements inherently discriminate against decay processes where the molecule does not dissociate, or where the molecule dissociates but one of the fragments is neutral.

Data analysis is essentially the same for both PIPICO and singles spectra. Spectra are taken at a number of photon energies in the Cl and S K-shell region. Peaks are integrated in order to determine fractional yields, or branching ratios, as a function of energy.

II. RESULTS AND DISCUSSION

A. HCl, DCl

A total-ion-yield spectrum for HCl near the chlorine K edge is shown in Fig 1. The molecular orbital notation for the ground-state electronic configuration of both HCl and DCl is

$$1\sigma^2 \ 2\sigma^2 \ 3\sigma^2 \ 1\pi^4 \quad \text{core shells}$$

$$4\sigma^2 \ 5\sigma^2 \ 2\pi^4 \ 6\sigma^{*0} \quad \text{valence shells.} \qquad (1)$$

The first spectral peak in Fig. 1 is attributed to a resonance transition from a chlorine 1s orbital to a $6\sigma^*$ antibonding orbital [5], which is comprised primarily of the atomic chlorine 3p and hydrogen 1s orbitals. The second peak in Fig. 1 results from a superposition of transitions to the Rydberg orbitals $7\sigma^*, 3\pi^*$, and $8\sigma^*$ derived from the Cl 4p and higher atomic orbitals.

Figure 6 shows fractional ion yields obtained from HCl and DCl singles spectra, whereas Fig. 7 shows fractional yields obtained from PIPICO spectra. As expected yields of
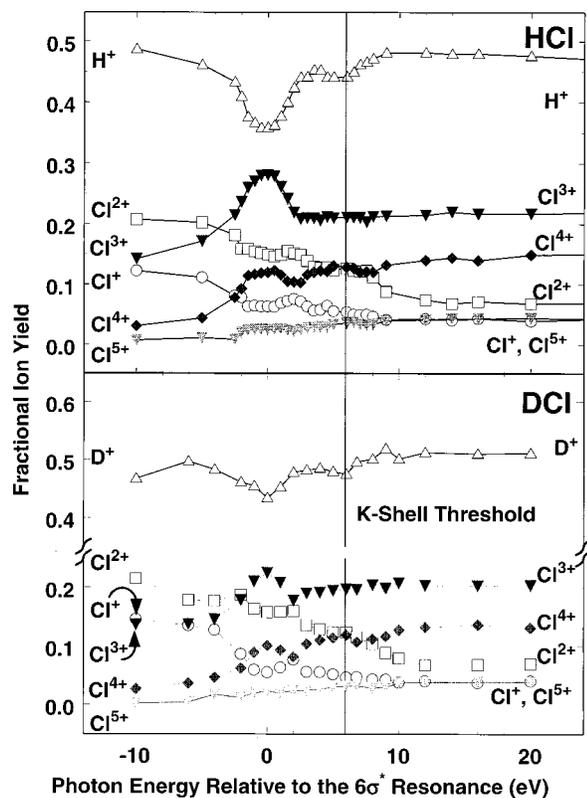
FIG. 6. Branching ratios as a function of energy for HCl and DCl singles spectra. The Cl^{6+} peak is omitted for clarity.

FIG. 7. Branching ratios as a function of energy for HCl and DCl PIPICO spectra. The Cl^{6+} peak is omitted for clarity.

the Cl^{3+}, Cl^{4+}, and Cl^{5+} charge states increase above threshold, while yields of Cl^{2+} and Cl^{+} decrease. In the region below the $1s \rightarrow 6\sigma^*$ resonance, changes in relative yields of different ionic states are visible in all of the fractional ion yields. The trend is reflected in the sharp increase in the average charge state (Fig. 8) at energies that are several linewidths below the resonance (linewidth is 1.86 eV [5]). We attribute this effect to pre-edge inner-shell photoionization [22], where the photoelectron is excited to the Lorentzian profile of a continuum state [23]. Previous studies have observed the onset of this effect tens of eV below the $1s \rightarrow 4p$ resonance in Ar [24] and for more than 10 eV below the first sulfur K-edge resonances in OCS and CS_2 [22].

The most prominent feature in Fig. 6, for both the HCl and DCl data, is the dip in the fraction of hydrogen produced on the $1s \rightarrow 6\sigma^*$ resonance, which has been attributed to production of neutral hydrogen [25]. The ratio of hydrogen ions to chlorine ions (Fig. 9) shows a drop in the hydrogen-to-chlorine ratio of 40% for HCl and 20% for DCl. Although DCl undergoes the same decay transitions as HCl, the amount of neutral hydrogen produced is less by about a factor of two due to the fact that the heavier deuterium cannot escape the attractive potential of a Cl^{+n} ion as quickly as the lighter hydrogen.

Immediately above the Cl $1s$ threshold, the fractional ion yields (Fig. 6) for Cl^{3+}, Cl^{4+}, Cl^{5+}, and H^+ increase while for Cl^{2+} there is a decrease in yield. The effect is particularly pronounced in the PIPICO yields. Similarly, the average charge state shows an increase in the same region (Fig. 8). These trends have been ascribed to postcollision interaction (PCI) [26], where the photoion can recapture the
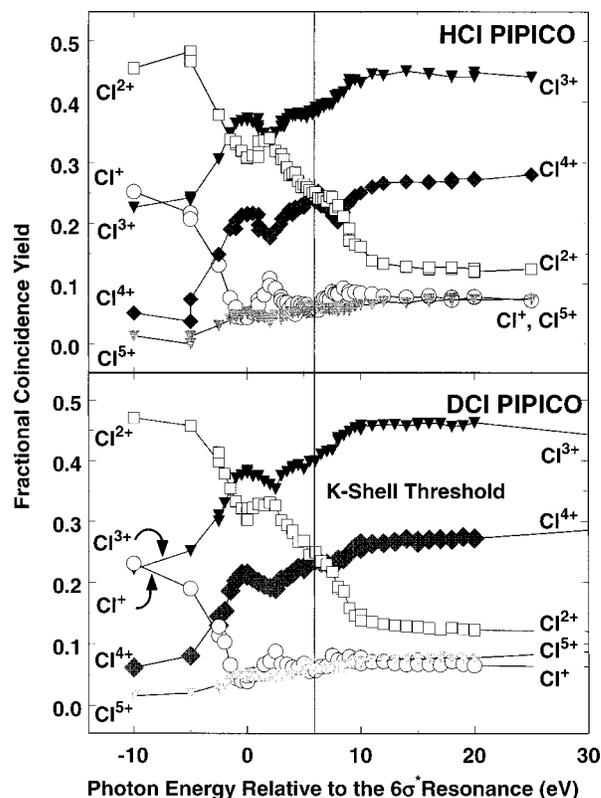
photoelectron following Auger decay.

Structure is also visible in the region between the first resonance and threshold. This is particularly true of the PIPICO yield curves. While yields of the higher charge states (Cl^{3+}, Cl^{4+}, Cl^{5+}) tend to follow the structure of the TIY spectrum, yields for the lower charge states (Cl^+, Cl^{2+}) follow the TIY inversely. This is a result of the fact that the lower charge states are produced primarily by valence photoionization, rather than K-shell photoionization. Because the cross section for K-shell photoexcitation increases dramati-
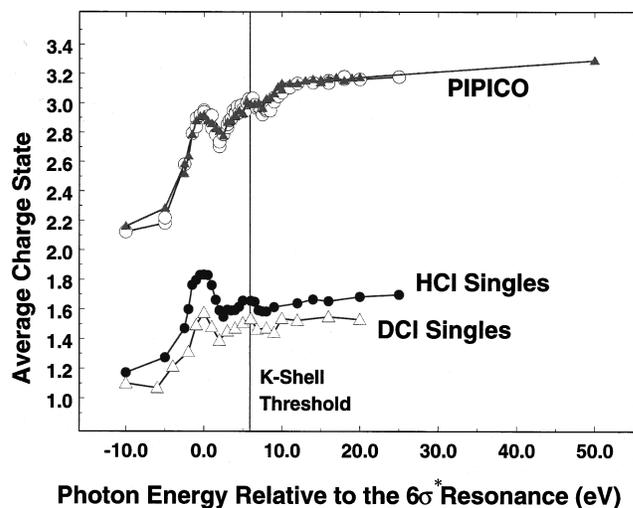

FIG. 8. Average chlorine charge state for HCl (circles) and DCl (triangles) singles and PIPICO spectra.
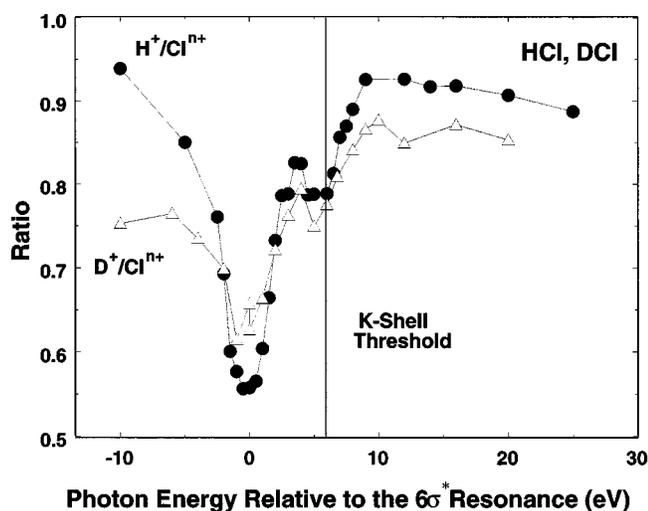
FIG. 9. Ratio of hydrogen (circles) or deuterium (triangles) ions detected to the sum of all chlorine ions in singles mode.

cally on resonance, the yields of the higher charge states increase, thus decreasing the fractional yield for the lower charge states. Between the first and second resonances, the opposite is true, and the lower K-shell cross section results in an increase in the fractional yields of Cl^+, Cl^{2+}. A similar effect is visible in the average charge curves (Fig. 8), where the subthreshold structure follows that of the absorption cross section.

Figure 10(a) shows the H^+ peaks from HCl singles spectra taken on the $6\sigma^*$ resonance and at 50 eV above resonance with the analyzer parallel to the orientation of the polarization vector of the SR. Areas in the peaks are normalized to one in order to obviate differences in the H^+ peak shape caused by changes in the β parameter or the amount of kinetic energy released as a function of photon energy. In this context, β is the parameter that describes the angular distribution of photofragments in the well-known expression for the differential photoionization cross section [27]

$$\frac{d\sigma}{d\Omega} = \frac{\sigma}{4\pi}\left[1 + \frac{\beta}{2}(3\cos^2\theta - 1)\right]. \qquad (2)$$

Here σ is the partial photoionization cross section, Ω is the solid angle, and θ is the angle between the ejected fragment and the polarization vector of the SR.

Within experimental error, both curves in Fig. 10(a) have the same baseline width, indicating that both are the result of fragments ejected with the same kinetic energy, and that differences in peak shapes are due to purely angular effects. These differences arise because of the well-defined symmetry of the resonantly excited orbital (i.e., $6\sigma^*$); molecules with their axes parallel to the polarization vector of the SR preferentially absorb incident photons. Following photoabsorption by HCl, the molecule will, in most cases, fragment, and because decay and dissociation of the molecule occur rapidly compared to molecular rotations, fragments are ejected parallel to the polarization vector. The double peaks reflect orientation of the molecule due to selective excitation. Because of its smaller mass, H^+ is ejected with a much higher velocity than Cl^{n+}; H^+ ions ejected toward and
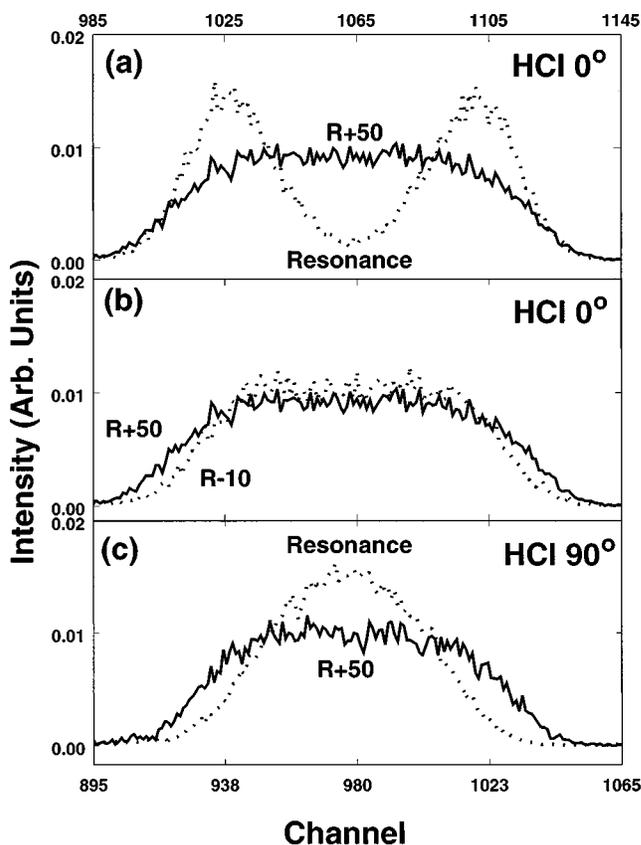

FIG. 10. H^+ peaks from HCl singles spectra. (a) Data taken on resonance (dotted line), and 50 eV above resonance (solid line) with the analyzer parallel to the polarization vector of the SR. (b) Data taken 10 eV below resonance (dotted), and 50 eV above resonance (solid) with the analyzer parallel to the polarization vector of the SR. (c) Data taken on resonance (dotted) and 50 eV above resonance (solid) with the analyzer perpendicular to the polarization of the SR. The labels on the top x axis correspond to the $0°$ plots, while labels on the bottom axis correspond to the $90°$ plot.

away from the detector contribute to the peaks at faster and slower flight times, respectively. The same effect was observed in ion-TOF studies of HCl after excitation of a Cl $2p$ electron [28].

The energy released in fragmentation (U_0) can be determined from the peak width using the expression [1]

$$U_0 = \left(\frac{qEt}{2}\right)^2 \frac{1}{2m}, \qquad (3)$$

where q, E, t, and m are the charge, electric field in the interaction region, peak width, and mass of the ion using SI units. Equation (3) assumes that fragments are perfectly space focused and that the electric field in the extraction region is uniform. Deviations from ideal conditions always increase the peak width, thus the values calculated are upper bounds. As a test, the widths of peaks in argon singles spectra were found to be about 0.1 eV. Because the broadening in argon can only be the result of instrumental broadening and thermal energy, these spectra provide a good measure of instrumental resolution, which in this case is much better than the error in the HCl data. For HCl, on resonance, the average energy released, as measured by the time between the

maxima of the peaks, is 11(2) eV, while the most energetic ions have an energy of about 48(4) eV.

Figure 10(b) shows H$^+$ peaks from HCl singles spectra taken 10 eV below and 50 eV above $1s \to 6\sigma^*$ resonance with the analyzer in the 0° orientation. It is clear that below resonance the H$^+$ peak is narrower than above resonance. At 50 eV above resonance, the H$^+$ peak has a width of 25(3) eV (FWHM), while the H$^+$ peak for the 10-eV-below spectrum is 18(2) eV wide (FWHM). An identical change in width is observed in spectra taken at the 90° orientation (not shown). This demonstrates that the change in peak width is a result of a change in the amount of kinetic energy released in fragmentation rather than an angular effect. This observation is in line with the fact that below the $6\sigma^*$ resonance and above the K-shell threshold we expect $\beta=0$. In both of these energy regimes we are dealing with excitations into the continuum, and thus there is no specific orbital symmetry to produce an aligned molecule. Finally, for comparison purposes, we note that the calculated value for the energy released due to the electrostatic repulsion between H$^+$ and Cl^{n+} is $n \times 11.3$ eV.

In order to gain a more quantitative description of dissociation, we treated the data to determine the β parameter on resonance. In order to do this, the ratio of the yield of H$^+$ on resonance to the yield of H$^+$ below resonance was determined. The areas of the H$^+$ peak on resonance [Fig. 10(a)] and below resonance [Fig. 10(b)] were normalized to this ratio, and their difference was taken in order to remove the effects of valence and shallow-core-level ionization. The background-subtracted peak was then fit accurately by two Gaussian peaks, indicating that the H$^+$ intensity is entirely a result of HCl molecules aligned with the polarization vector of the SR. Therefore for resonantly excited molecules, $\beta = 2$ within experimental error. Figure 10(c) shows the H$^+$ peaks from TOF spectra taken on the $6\sigma^*$ resonance and at 50 eV above resonance with the analyzer perpendicular to the polarization vector of the SR. The resonant H$^+$ peak is significantly narrower than the 50 eV above resonance peak. In this orientation, the H$^+$ peak maintains the same width in both on resonance, and below resonance spectra. This is as we would expect for $\beta = 2$ since with the analyzer in this orientation, the resonantly excited molecules are aligned with their bond axes perpendicular to the analyzer axis, and the kinetic energy released in fragmentation has no effect on the ion flight times.

B. H$_2$S, D$_2$S

Figure 4 shows a total-coincidence-yield spectrum for H$_2$S. The ground-state electronic configuration of H$_2$S is

$$1a_1^2 \; 2a_1^2 \; 1b_2^2 \; 3a_1^2 \; 1b_1^2 \quad \text{core shells}$$

$$4a_1^2 \; 2b_2^2 \; 5a_1^2 \; 2b_1^2 \quad \text{valence shells}$$

$$3b_2^0 \; 6a_1^0 \quad \text{empty shells.} \tag{4}$$

The first peak in Fig. 4 is attributed [6,7] to the excitation of electrons from the sulfur $1s$ to the $3b_2$ (derived from hydrogen $1s$ and sulfur $3p_x$) and $6a_1$ (derived from the hydrogen $1s$ and sulfur $3s$, $3p_z$, $3d$) antibonding molecular orbitals.
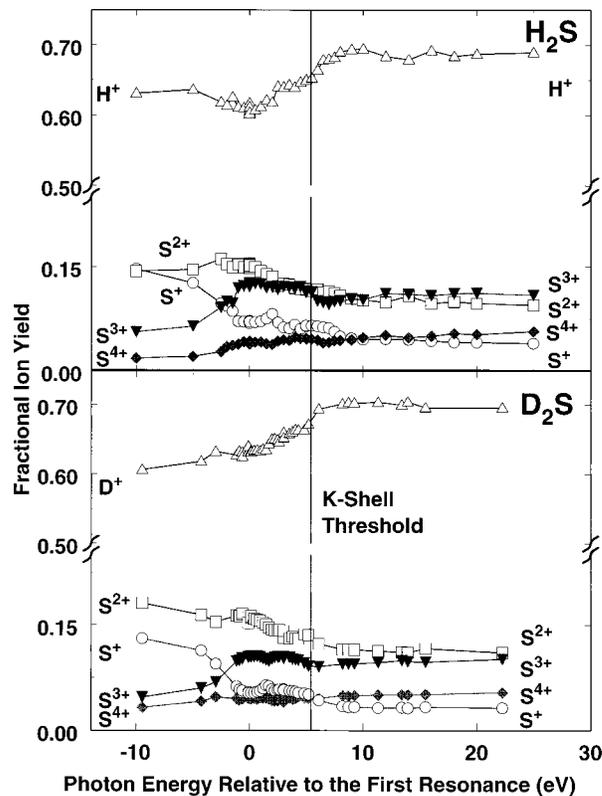

FIG. 11. Branching ratios as a function of energy for H$_2$S and D$_2$S singles spectra. The S^{5+} peak is omitted for clarity.

As a result of dipole matrix elements, the contribution of the a_1 orbital is only about 20% of the b_2 orbital [6]. The two resonances are separated by only 0.5 eV [29] and are unresolved due to lifetime broadening from the energy levels (0.3–0.5 eV), the photon energy width (≈ 0.4 eV), and the Franck-Condon effect [7]. The second peak in Fig. 4 is attributed to excitations from the sulfur $1s$ to the $4b_1$, $4b_2$, and $8a_1$ orbitals [5]. Finally, for H$_2$S a third peak, just below threshold, resulting from transitions to $5p$ derived Rydberg orbitals [30] is visible in the TCY spectrum.

In the singles data for both H$_2$S and D$_2$S (Fig. 11), the branching ratios are nearly identical. As the photon energy increases from below resonance to above the K-shell threshold, the fractional yields for S^{3+} and S^{4+} increase while the yields for S$^+$ and S^{2+} decrease. The only notable difference between the H$_2$S and D$_2$S data is a decreased D$^+$ yield below resonance, which is at least partially a result of a larger yield for the molecular ion DS$^+$ at below-resonance energies. In addition, trends in the average sulfur charge state (Fig. 12) are nearly identical for both H$_2$S and D$_2$S and show a similar, although different in magnitude, enhancement on resonance when compared to the average Cl charge state in HCl and DCl (Fig. 8). Again, a sharp increase in the average charge state below resonance indicates the onset of pre-edge inner-shell ionization.

On the lowest resonance Fig. 11 shows a depletion in the H$^+$ yield. As with HCl, we attribute this to neutral dissociation of hydrogen. In this energy range the magnitude of the DS$^+$ peak in the spectra indicates that this is not a result of an increased molecular ion yield. Furthermore, the charge states that show an enhanced yield on resonance relative to
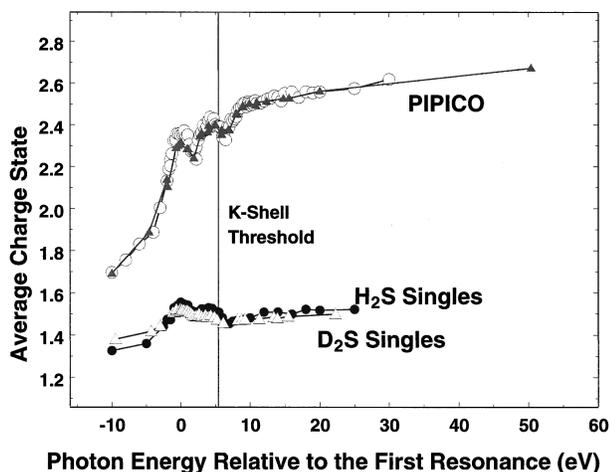
FIG. 12. Average sulfur charge state for H_2S (circles) and D_2S (triangles) singles and PIPICO spectra.

FIG. 14. Ratio of hydrogen (circles) or deuterium (triangles) ions detected to the sum of all sulfur ions detected in singles mode.

their above-threshold values in the singles spectra (Fig. 11) show a smaller yield on resonance than above threshold in the PIPICO spectra (Fig. 13). For both H_2S and D_2S, Fig. 14 shows that about 30% less H^+ is detected on resonance than above threshold.

Because H_2S is a triatomic molecule, the dissociation picture is slightly more complicated than in HCl. Auger decay competes with dissociation of not just one but possibly both hydrogen atoms:
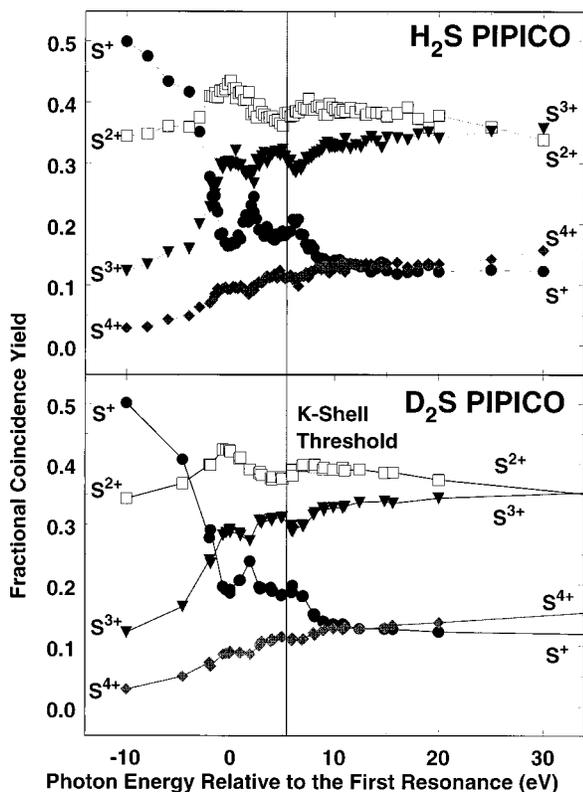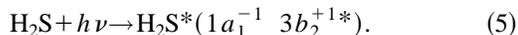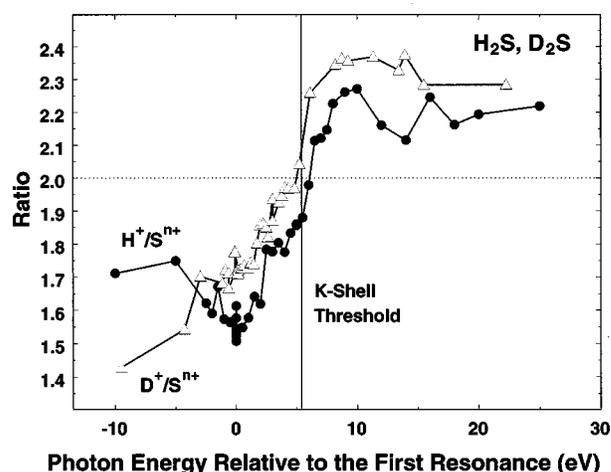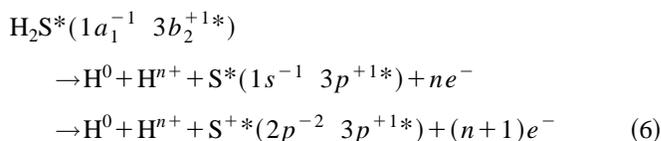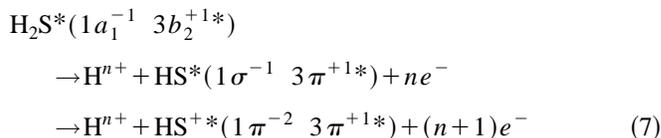
$$H_2S + h\nu \rightarrow H_2S^*(1a_1^{-1} \ 3b_2^{+1}*). \quad (5)$$

FIG. 13. Branching ratios as a function of energy for H_2S and D_2S PIPICO spectra. The S^{5+} peak is omitted for clarity.

In Eq. (5) the notation $3b_2^{+1}$ is shorthand for excitation into either the $3b_2$ or $6a_1$ orbital. The key point in this discussion is to delineate the different possible mechanisms in which molecular dissociation will compete with Auger decay. In the first mechanism

$$H_2S^*(1a_1^{-1} \ 3b_2^{+1}*)$$
$$\rightarrow H^0 + H^{n+} + S^*(1s^{-1} \ 3p^{+1}*) + ne^-$$
$$\rightarrow H^0 + H^{n+} + S^{+*}(2p^{-2} \ 3p^{+1}*) + (n+1)e^- \quad (6)$$

we have dissociation of both hydrogens prior to Auger decay, and one or both of the hydrogens are neutral ($n=0$ or 1). Alternatively,

$$H_2S^*(1a_1^{-1} \ 3b_2^{+1}*)$$
$$\rightarrow H^{n+} + HS^*(1\sigma^{-1} \ 3\pi^{+1}*) + ne^-$$
$$\rightarrow H^{n+} + HS^{+*}(1\pi^{-2} \ 3\pi^{+1}*) + (n+1)e^- \quad (7)$$

one hydrogen dissociates prior to the Auger decay, and the other dissociates after Auger decay, with at least one dissociating as a neutral, or

$$H_2S^*(1a_1^{-1} \ 3b_2^{+1}*) \rightarrow H_2S^{+*}(1b_m^{-2} \ 3b_2^{+1}*) + e^-, \quad (8)$$
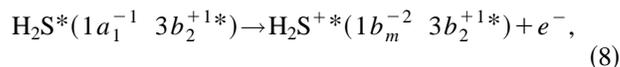
where dissociation of both hydrogens occurs following the Auger decay of the $1s$ hole in the molecule, and $1b_m$ is shorthand for the $1b_1$ and $1b_2$ molecular orbitals derived from the S $2p$ atomic orbitals. Again, as in the chlorine case, $2p$-derived holes also will subsequently relax, typically through Auger decay.

Ab initio studies [31] show that for _L_-shell decay there is only a very small contribution from the decay channel that involves dissociation of both hydrogens prior to autoionization. This is due to the relatively high cost in energy that this process requires. Furthermore, electron-spectroscopy studies [10,11] of the decay of _L_-shell holes in H_2S show that the primary channel involves dissociation of one hydrogen atom followed by Auger decay from the excited HS molecule. The present data do not allow us to determine if the shorter _K_-

hole lifetime is sufficient to cause a change in the primary decay path when compared to the *L*-core hole. Further studies will be required to determine if the antibonding orbital is repulsive enough to cause neutral fragmentation on a shorter time scale than the lifetime of the *K*-shell hole.

Previous studies [26] have shown that when HCl fragments into H^+ and Cl^{n+} the decay process can be similar to that for the $Ar^{(n+1)+}$ ion. The data suggest that a similar analogy can be made between the Cl^{n+} ion and the $S^{(n-1)+}$ ion. The singles fractional ion yield for S^{3+} (Fig. 11) shows an enhancement on both the first and Rydberg resonances in a manner that is qualitatively similar to Cl^{4+} in HCl (Fig. 6). Thus it seems likely that the relaxation pathways that enhance the Cl^{4+} yield following resonant excitation are analogous to those causing enhancement in the S^{3+} yield. For S^{2+}, the fractional yield from the singles spectra (Fig. 11) shows only a slight resonant enhancement, while the PIPICO spectra (Fig. 13) show a distinct enhancement in yield on the $6a_1$-$3b_2$ resonance, indicating that at least one of the hydrogens fragments as H^+. If the other hydrogen fragments as a neutral, the increase in the S^{2+} PIPICO yield (Fig. 13) can be explained as analogous to the enhanced Cl^{3+} yield (Fig. 6) upon excitation to the lowest unoccupied molecular orbital.

The $I(H^+)/I(Cl^{n+})$ and $I(H^+)/I(S^{n+})$ ratios (Figs. 9 and 14) also point out inherent uncertainties in data collection. Above threshold, where the molecules are nearly completely fragmented, the $I(H^+)/I(Cl^{n+})$ ratio should be one, and the $I(H^+)/I(S^{n+})$ ratio should be two. However, in the present experimental setup, only one ion from a fragmentation event is detected. Both the H^+ and its sister ion (Cl^{n+} or S^{n+}) from the same molecule have approximately equal probabilities to reach the detector. However, because of its smaller mass, the H^+ ion will reach the detector first. If the H^+ ion is detected, no more ions will be detected from that fragmentation event. Thus Cl^{n+} or S^{n+} has a smaller probability of being detected dependent on the detection efficiency for H^+. This effect is in competition with a slightly smaller extraction efficiency for the H^+ ions. Earlier we mentioned that all H^+ ions created at the tip of the gas needle with an energy of less than 50 eV would be collected. In practice, because the photon beam traverses the entire aperture, not all H^+ ions are created at the tip of the needle, and some are lost. It appears that for HCl (Fig. 9), the second effect dominates as evidenced by the fact that the above-threshold ratio is <1. On the other hand, for H_2S, the faster H^+ flight time and the fact that there are two H^+ ions causes some discrimination against the S^{n+} ion causing $I(H^+)/I(S^{n+}) > 2$.

Figures 15(a) and 15(b) show H^+ peaks from singles spectra of H_2S taken with the analyzer oriented parallel to the polarization vector of the SR, while Fig. 15(c) shows H^+ peaks taken with the analyzer in the perpendicular orientation. The data are shown from spectra taken 50 eV above, 10 eV below, and on the $6a_1$,$3b_2$ resonance. The peaks in these spectra show an asymmetry with the right side (shorter flight time) having a higher intensity. This can be explained by the fact that when H_2S fragments, one of the H^+ ions will reach the detector faster than the other. If the faster H^+ ion is detected, it will not be possible for the slower H^+ ion to be
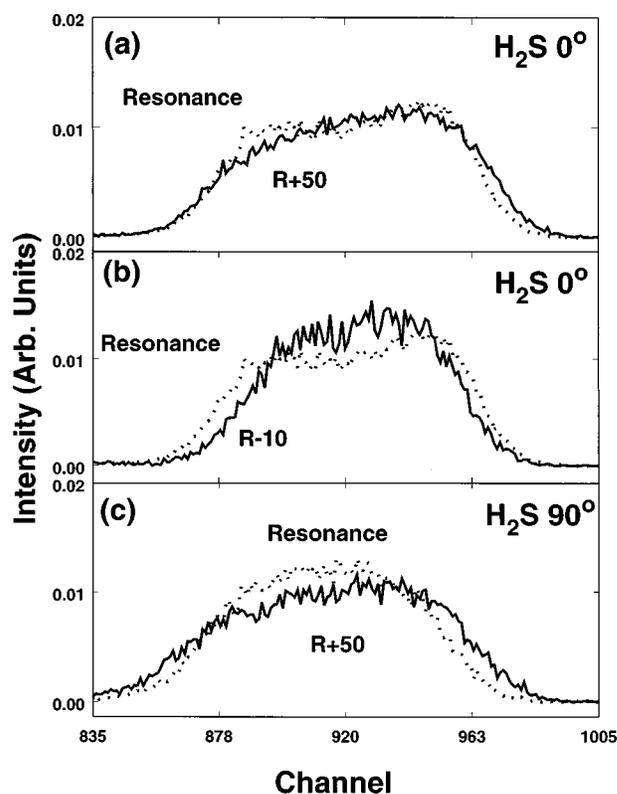

FIG. 15. H^+ peaks from H_2S singles spectra. (a) Data taken on resonance (dotted) and 50 eV above resonance (solid) with the analyzer parallel to the polarization vector of the SR. (b) Data taken 10 eV below resonance (solid), and on resonance (dotted) with the analyzer parallel to the polarization vector of the SR. (c) Data taken on resonance (dotted) and 50 eV above resonance (solid) with the analyzer perpendicular to the polarization of the SR.

detected, resulting in discrimination against the slower H^+ ion and the difference in intensity [32].

Trends in the widths of the hydrogen peaks in these spectra are similar to those observed for HCl. For the parallel orientation, within experimental error, the widths of the on-resonance and above-resonance H^+ peaks are identical [15(2) eV and 17(2) eV FWHM, respectively], while the below-resonance peak is narrower [11(2) eV FWHM]. Furthermore, for spectra taken in the perpendicular orientation the H^+ peaks from the on-resonance and below-resonance spectra are nearly identical in width [13(2) eV FWHM] while the above-resonance H^+ peak is wider [18(2) eV FWHM, Fig. 15(c)]. The fact that H_2S is a ''bent'' triatomic molecule with C_{2v} symmetry, and the fact that the first resonant peak is the result of excitations to two orbitals of different symmetry ($6a_1$ and $3b_2$) makes data interpretation more difficult. However, the data presented here are consistent with previous *K*-shell measurements of H_2S, which report a positive β on the $6a_1$,$3b_2$ resonance [33].

Following excitation of a *K*-shell electron by an incident photon, a high degree of molecular fragmentation, and fragment (chlorine or sulfur) ionization of the atom was observed in HCl, DCl, H_2S, and D_2S. On resonance, a positive β was observed, as well as a significant decrease in the yield of hydrogen detected. Resonant decreases in H^+ yields are attributed to increases in the amounts of neutral hydrogen created. These increases in the production of neutral hydrogen

correspond to increases in Cl^{3+} or S^{2+} yields. Because these are the first studies of this type on these molecules at K-shell energies, a number of questions remain. Electron-spectroscopy studies of these molecules will be required to elucidate the multitude of decay paths and determine if fragmentation of the molecule occurs on the same time scale as Auger decay of the deep-inner-core hole. In addition, evidence was found for the occurrence of pre-edge ionization of a K-shell electron below resonance, as well as postcollision-interaction effects in the energy regimes immediately above the K-shell threshold.

[1] W. C. Wiley and I. H. McLaren, Rev. Sci. Instrum. **26**, 1150 (1955).

[2] J. Jauhiainen, S. Aksela, and E. Nõmmiste, Phys. Scr. **51**, 549 (1995).

[3] J. H. D. Eland, Acc. Chem. Res. **22**, 381 (1989).

[4] T. A. Carlson and M. O. Krause, Phys. Rev. **137**, A1655 (1965).

[5] S. Bodeur, J. L. Maréchal, C. Reynaud, D. Bazin, and I. Nenner, Z. Phys. D **17**, 291 (1990).

[6] S. Bodeur and J. M. Esteva, Chem. Phys. **100**, 415 (1985).

[7] R. E. LaVilla, J. Chem. Phys. **62**, 2209 (1975).

[8] H. Aksela, S. Aksela, M. Ala-Korpela, O-P. Sairanen, M. Hotokka, G. M. Bancroft, K. H. Tan, and J. Tulkki, Phys. Rev. A **41**, 6000 (1990).

[9] A. Menzel, B. Langer, J. Viefhaus, S. B. Whitfield, and U. Becker, Chem. Phys. Lett. **258**, 265 (1996).

[10] H. Aksela, S. Aksela, A. Naves de Brito, G. M. Bancroft, and K. H. Tan, Phys. Rev. A **45**, 7948 (1992).

[11] A. Naves de Brito, N. Correia, B. Wannberg, P. Baltzer, L. Karlsson, S. Svensson, M. Y. Adam, H. Aksela, and S. Aksela, Phys. Rev. A **46**, 6067 (1992).

[12] E. Kukk, A. Wills, N. Berrah, B. Langer, J. D. Bozek, O. Nayandin, M. Alsherhi, A. Farhat, and D. Cubaynes, Phys. Rev. A **57**, R1485 (1998).

[13] J. C. Levin, D. W. Lindle, N. Keller, R. D. Miller, Y. Azuma, N. Berrah Mansour, H. G. Berry, and I. A. Sellin, Phys. Rev. Lett. **67**, 968 (1991).

[14] D. W. Lindle, W. L. Manner, L. Steinbeck, E. Villalobos, J. C. Levin, and I. A. Sellin, J. Electron Spectrosc. Relat. Phenom. **67**, 373 (1994).

[15] J. C. Levin, C. Biedermann, N. Keller, L. Liljeby, C.-S. O, R. T. Short, I. A. Sellin, and D. W. Lindle, Phys. Rev. Lett. **65**, 988 (1990).

[16] G. Jones, S. Ryce, D. W. Lindle, B. A. Karlin, J. C. Woicik, and R. C. C. Perera, Rev. Sci. Instrum. **66**, 1748 (1995).

[17] R. C. C. Perera, G. Jones, and D. W. Lindle, Rev. Sci. Instrum. **66**, 1745 (1995).

[18] W. Ng, G. Jones, R. C. C. Perera, D. Hansen, J. Daniels, O. Hemmers, P. Glans, S. Whitfield, H. Wang, and D. W. Lindle, Rev. Sci. Instrum. **67**, 1 (1996).

[19] P. L. Cowan, S. Brennan, R. D. Deslattes, A. Henins, T. Jach, and E. G. Kessler, Nucl. Instrum. Methods Phys. Res. A **246**, 154 (1986).

[20] P. L. Cowan, S. Brennan, T. Jach, D. W. Lindle, and B. A. Karlin, Rev. Sci. Instrum. **60**, 1603 (1989).

[21] B. Esser, U. Ankerhold, N. Anders, and F. von Busch, J. Phys. B **30**, 1191 (1997).

[22] F. von Busch, U. Ankerhold, S. Drees, and B. Esser, J. Phys. B **29**, 5343 (1996).

[23] M. Y. Amusia, Phys. Lett. A **183**, 201 (1993).

[24] J. Doppelfeld, N. Anders, B. Esser, F. von Busch, H. Scherer, and S. Zinz, J. Phys. B **26**, 445 (1993).

[25] D. L. Hansen, M. E. Arrasate, J. Cotter, G. R. Fisher, K. T. Leung, J. C. Levin, R. Martin, P. Neill, R. C. C. Perera, I. A. Sellin, M. Simon, Y. Uehara, B. Vanderford, S. B. Whitfield, and D. W. Lindle, Phys. Rev. A **57**, 2608 (1998).

[26] D. L. Hansen, G. B. Armen, M. E. Arrasate, J. Cotter, G. R. Fisher, K. T. Leung, J. C. Levin, R. Martin, P. Neill, R. C. C. Perera, I. A. Sellin, M. Simon, Y. Uehara, B. Vanderford, S. B. Whitfield, and D. W. Lindle, Phys. Rev. A **57**, R4090 (1998).

[27] S. T. Manson and D. Dill, in *Electron Spectroscopy: Theory, Techniques and Applications,* edited by C. R. Brundle and A. D. Baker (Academic, New York, 1978), Vol. 2, p. 157.

[28] H. Aksela, S. Aksela, M. Hotokka, A. Yagishita, and E. Shigemasa, J. Phys. B **26**, 3357 (1992).

[29] R. Mayer, D. W. Lindle, S. H. Southworth, and P. L. Cowan, Phys. Rev. A **43**, 235 (1991).

[30] E. Hudson, D. A. Shirley, M. Domke, G. Remmers, and G. Kaindl, Phys. Rev. A **49**, 161 (1994).

[31] A. Naves de Brito and H. Ågren, Phys. Rev. A **45**, 7953 (1992).

[32] N. Saito and I. H. Suzuki, J. Phys. B **22**, 3973 (1989).

[33] J. Adachi, Y. Takata, N. Kosugi, E. Hiraya, E. Shigemasa, A. Yagishita, and Y. Kitajima, Photon Factory Activity Rep. **14**, 14 (1996).